10-2015

The Unusual 3D Interplay of Basement Fault Reactivation and Fault-Propagation-Fold Development: A Case Study of the Laramide-age Stillwell Anticline, West Texas (USA)

Benjamin E. Surpless
Trinity University, bsurples@trinity.edu

Nicola Hill
Trinity University, nhill2@trinity.edu

Cara Beasley
Trinity University, cbeasley@trinity.edu

Repository Citation

Surpless, B., Hill, N., & Beasley, C. (2015). The unusual 3D interplay of basement fault reactivation and fault-propagation-fold development: A case study of the Laramide-age Stillwell anticline, west Texas (USA). *Journal of Structural Geology, 79*, 42-56. doi: 10.1016/j.jsg.2015.07.003

Journal of Structural Geology 79 (2015) 42–56

Contents lists available at ScienceDirect

Journal of Structural Geology

journal homepage: www.elsevier.com/locate/jsg

The unusual 3D interplay of basement fault reactivation and fault-propagation-fold development: A case study of the Laramide-age Stillwell anticline, west Texas (USA)

Ben Surpless*, Nicola Hill, Cara Beasley

Trinity University, 1 Trinity Place, San Antonio, TX 78212, USA

ARTICLE INFO

Article history:
Received 30 March 2015
Received in revised form
30 June 2015
Accepted 3 July 2015
Available online 7 July 2015

Keywords:
Stillwell anticline
Fault reactivation
Fault-propagation fold
En echelon
Kinematic modeling

ABSTRACT

Subsurface fault geometries have a systematic influence on folds formed above those faults. We use the extraordinarily well-exposed fold geometries of the Laramide-age Stillwell anticline in west Texas (USA) to develop a strain-predictive model of fault-propagation fold formation. The anticline is a 10-km long, NW-trending, NE-vergent, asymmetric fold system with an axis that displays a map-view left-stepping, en echelon pattern. We integrated field observations, geologic and structural data, cross-sections, and 2D kinematic modeling to establish an unusual 3D two-stage model of contractional fold formation, including: 1) reverse reactivation of a pre-existing, NW-striking, SW-dipping, left-stepping, en echelon normal fault system in Paleozoic basement rocks to generate monoclinal flexures in overlying layered Cretaceous carbonate rocks; and 2) the formation of a subsequent flat-ramp fault system that propagated horizontally along a mechanically-weak, clay-rich Cretaceous unit before ramping up at the hinge of the pre-existing monocline system. Strain is focused within the forelimb of the system, in front of the propagating fault tip, and is accommodated by a combination of interlayer slip, flat-ramp faulting, and fracturing proximal to planes of slip. This strain predictive model can be applied to similar, less-well-exposed contractional systems worldwide and provides a new, unusual example of Laramide-age contractional deformation.

1. Introduction

Many studies have demonstrated that fault geometries have a strong and systematic influence on the shapes of folds above to those fault systems (e.g., Suppe, 1985; Mitra, 1990; Erslev and Rogers, 1993; Rowan and Linares, 2000; Almendinger and Shaw, 2000; Wilkerson et al., 2002; and Savage and Cooke, 2003; Jabbour et al., 2012). Where fault systems are unexposed or only poorly defined, workers can utilize geometries of overlying folds to resolve the geometries of those fault systems; these subsurface fault geometries have significant impacts on the assessment of seismic hazard and the evaluation of fluid flow in the subsurface. In this investigation, we combine field-based data collection, structural analysis of complex map-view fold geometries, cross-section construction and analysis, and two-dimensional forward kinematic modeling to develop a viable fault-propagation fold evolution that reveals vital information about subsurface structure.

Our investigation of the Stillwell anticline, an unusually well-exposed northwest-trending structure in the northern Sierra Del Carmen of the Trans-Pecos region of west Texas, also provides new data that improve our understanding of variations in Laramide deformation along the geologically-complex orogenic belt (Fig. 1). Although contractional deformation associated with the Late Cretaceous – Early Paleogene Laramide orogeny has been well-studied in Montana, Wyoming, Colorado, and New Mexico, where workers have clearly demonstrated basement involvement in the formation of folds and faults (e.g., Chapin and Cather, 1983; Gries, 1983; Jacob and Albertus, 1985; Woodward, 1986; Miller et al., 1992), few studies examine Laramide structures in areas further south, especially near the eastern margin of Laramide deformation (Cobb and Poth, 1980; Muehlberger, 1980; Moustafa, 1983, 1988; Muehlberger and Dickerson, 1989; Carpenter, 1997).

We here provide a model of fault-propagation fold evolution that explains the formation of the complex Stillwell anticline system in the context of previous studies of similar systems (e.g.,

* Corresponding author. Dept. of Geosciences, Trinity University, 1 Trinity Place, San Antonio, TX 78209, USA.
E-mail address: bsurples@trinity.edu (B. Surpless).

http://dx.doi.org/10.1016/j.jsg.2015.07.003
0191-8141/

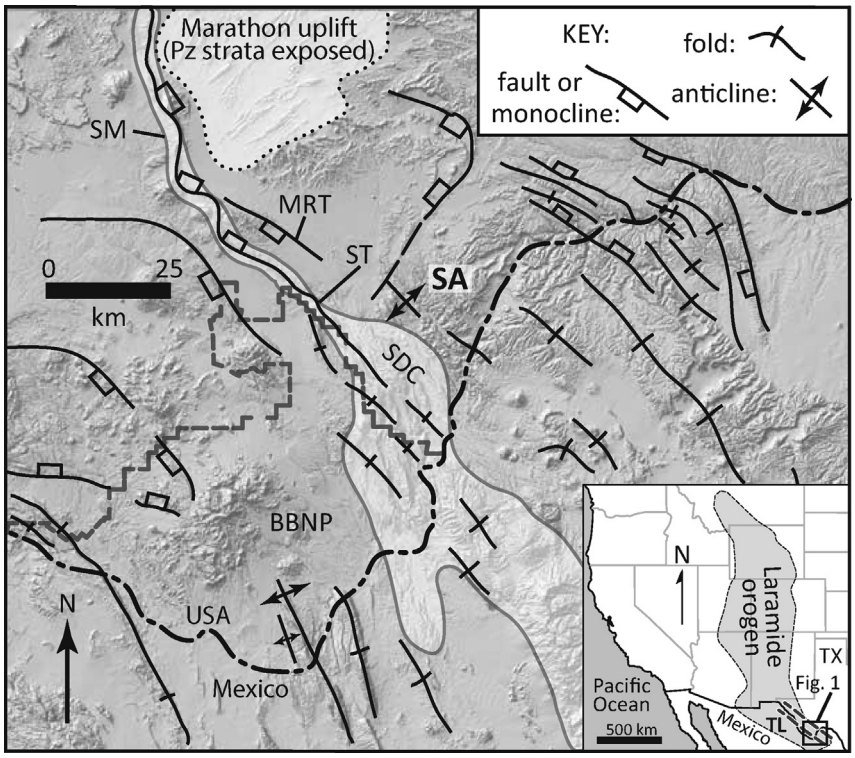

Fig. 1. Shaded relief map with major Laramide-age faults and folds of the Big Bend region, with inset (lower right) showing distribution of deformation associated with the Laramide orogen and the approximate boundaries of the Texas Lineament (TL). The Sierra del Carmen (SDC) and the Santiago Mountains (SM) are shaded in light gray. Big Bend National Park (BBNP) is outlined by a dashed, dark gray line. The Santiago thrust (ST) and the Maravillas Ridge thrust (MRT) are subparallel to the Stillwell anticline (SA). For most Laramide age folds, fold type is not differentiated. The rectangle on thrust faults/monoclines indicates the upthrown side of the fault/monocline system. Distribution of Laramide-age faults and folds modified from Muehlberger and Dickerson (1989) and Page et al. (2008). Laramide orogeny modified from Miller et al. (1992). Approximate boundaries of the Texas Lineament modified from Muehlberger (1980).

Suppe, 1985; Mitra, 1990; Suppe and Medwedeff, 1990; Erslev and Rodgers, 1993; Hardy and Ford, 1997; Mercier et al., 1997; Allmendinger, 1998; Jabbour et al., 2012). Our results suggest that the Stillwell anticline system formed in an unusual way relative to most other contractional fold systems worldwide. The documented anticline geometries were formed by two temporally-distinct styles of folding associated with Laramide-age compression: 1) initial compressional stresses reactivated a left-stepping, en echelon, high-angle basement fault system in pre-Mesozoic basement units, resulting in monoclinal structures in the layered carbonate rocks above the upward propagating faults; and 2) continued compression across the region resulted in the initiation of a separate, spatially- and temporally-distinct fault – propagation event, with a subhorizontal fault that propagated along a mechanically weak unit before ramping up at the hinge of the earlier monocline, creating a complex, but well-defined, fold geometry that varies along the axial trace of the system.

Importantly, we document outcrop-scale contractional strain of layered carbonates in the context of fault-propagation fold formation, tying the intensity of faults, interlayer slip, and fractures to the zone of greatest shear strain in front of the propagating fault tip. The predictive model we present here deepens our understanding of coupled fault-fold formation and provides a new and unusual example of how strain can be accommodated on the margins of continent-scale contractional deformation (Fig. 1). This model can be applied to coupled fault-fold systems worldwide, especially where data are not as complete.

2. Background

2.1. Pre-Laramide tectonics of Big Bend region

The Stillwell anticline is located within the Texas Lineament, an 80-km wide, northwest-trending zone of deformation (e.g., Albritton and Smith, 1957; Sears and Price, 1978; Muehlberger, 1980; TL in Fig. 1) thought to be fundamentally influenced by earlier plate-scale tectonic events which affected the Big Bend Region beginning in the Middle Proterozoic (e.g., Sears and Price, 1978; Muehlberger, 1980; Maler, 1990; Page et al., 2008; Thomas, 2011). The orientation of transform faults relating to Neoproterozoic rifting are subparallel to the NW-trending lineament (Thomas, 1991; Poole et al., 2005), which is considered a fundamental crustal weakness that juxtaposes the original craton to the northeast against accreted terranes to the southwest (e.g., Muehlberger, 1980; Page et al., 2008; Thomas, 2011). Late Paleozoic extensional deformation and uplift resulted in high-angle, northwest-striking normal faults to the north and northwest (e.g., Muehlberger, 1980 *and refs. therein*; Henry, 1998). During this period of Late Paleozoic deformation, the Big Bend region was part of the uplifted Diablo platform, adjacent to the Delaware basin (e.g., Henry, 1998; Goldhammer and Johnson, 1999; Page et al., 2008), but any normal fault systems associated with this event are obscured in the Stillwell anticline region by the deposition of Mesozoic marine strata.

Rifting between South and North America and the opening of the Gulf of Mexico likely affected the Diablo platform from the Late Triassic into the Late Cretaceous (e.g., Muehlberger, 1980; Muehlberger and Dickerson, 1989; Lehman and Busbey, 2007; Page et al., 2008), resulting in regional deposition of Lower to mid-Cretaceous limestone, clay, and siltstone strata in a shallow marine setting (e.g., St. John, 1965; Maxwell et al., 1967; Page et al., 2008). Subsidence and marine deposition came to an end in the Big Bend Region by Late Cretaceous time, when Laramide compression began to affect the area (e.g., Lehman and Busbey, 2007; Page et al., 2008).

2.2. Laramide-age contractional deformation and the Stillwell anticline

As the rate of convergence between the Farallon and North American plates increased in the Cretaceous, Sevier and later Laramide compression affected much of the western U.S. (Fig. 1, inset; e.g., Coney and Reynolds, 1977; Dickinson, 1981; Miller et al., 1992). Laramide-style deformation is best characterized by basement-cored uplifts of pre-fractured anisotropic basement blocks (e.g., Miller et al., 1992 and references therein; Liu et al., 2010). Although the thickness and structural anisotropy of basement vary from one area of Laramide deformation to another, these pre-existing basement structures localized much of the deformation, reactivating structural trends with long histories of recurrent movement (e.g., Tweto, 1975; Allmendinger, 1992). Most basement-involved, fault-related anticlines of the Laramide orogeny are characterized by thinned, steeply-dipping forelimbs and gently-to moderately-dipping backlimbs (e.g., Stone, 1993).

Laramide-age faults and folds in some areas of the Big Bend region were generated in two episodes from the latest Cretaceous through the early Eocene, with the maximum compressive stress shifting from northeast to a dominantly east-northeast orientation (e.g., Berge, 1981; Henry and Price, 1985; Price and Henry, 1988; Cullen et al., 2013). This period of deformation, based on evidence from sedimentological and tectonic studies, began at 70–65 Ma and ended after the middle Eocene, at about 50 Ma (Lehman, 1991; Lehman and Busbey, 2007; Page et al., 2008). In the eastern Big Bend region, which includes the Stillwell anticline, Laramide folds and faults most commonly trend northwest, subparallel to the structural grain of the Texas Lineament (e.g., Abritton and Smith, 1957; Muehlberger, 1980; Moustafa, 1988). However, the orientation of tectonic stylolites and the analysis of slickenside striations on exposed thrust faults near the Stillwell anticline support an ENE-directed maximum compressive stress orientation when these structures formed (Maxwell et al., 1967; Moustafa, 1983, 1988; Maler, 1990). Therefore, the northwest − trending Laramide monoclines and anticlines, including the Stillwell anticline, were at an oblique angle relative to the maximum compressive stress, resulting in left-lateral transpression (e.g., Moustafa, 1983, 1988; Maler, 1990).

Previous studies of the geometry of the asymmetric, northeast-vergent Stillwell anticline suggest a reverse fault origin (e.g., St. John, 1965; Surpless and Quiroz, 2010; Mays et al., 2012; Surpless and DeZoeten, 2013), broadly similar in orientation to other Laramide-age structures in the region (Fig. 1; e.g., Muehlberger, 1980; Moustafa, 1988; Maler, 1990; Carpenter, 1997), including the Santiago thrust (ST in Fig. 1) and the Maravillas Ridge thrust (MRT in Fig. 1). The Laramide fault and fold distribution of Muehlberger and Dickerson (1989) shown in Fig. 1 suggests that the north end of the anticline is truncated by a northeast − trending fault, and structural evidence and topographic expression of the fold disappear approximately 10 km south of this hypothesized truncation. The well-described and simple stratigraphy of the area (e.g., St. John, 1965, 1966; Maxwell et al., 1967), drainage systems that cut through the fold system to expose cross-sectional views of fold geometries, and nearly complete bedrock exposure permit a well-constrained, three-dimensional investigation of fold development. Although the transition from contractional deformation to Basin and Range extension occurred sometime between 47 Ma (e.g., Miggins, 2009) and 30 Ma (e.g., Henry et al., 1983; Price and Henry, 1984; Henry and Price, 1986), there are no significant normal faults in the Stillwell anticline map area (St. John, 1966; Moustafa, 1988; this study).

2.3. Kinematic models of fault-propagation folding

Complete cross-sectional exposures or seismic images of fault propagation folds are rare, so geologists have developed models to constrain these fold systems, especially in the context of progressive slip on the underlying fault system (Fig. 2). The kink-band model (e.g., Suppe, 1983) has proven a powerful tool to quantitatively analyze fault-propagation fold systems in many cases (e.g., Chester and Chester, 1990; Suppe and Medwedeff, 1990; Mercier et al., 1997). In this model, as slip increases on the underlying fault, backlimb length (A–A′ in Fig. 2A) increases, middle limb length (A′ − B in Fig. 2A) decreases, and fold amplitude increases. However, the fold shape and position remain constant relative to the propagating fault tip during progressive deformation (self-similar fold development) (Fig. 2A), a behavior that deviates from many natural fault-propagation fold systems. Other workers have developed models where the fold interlimb angle tightens with progressive shortening and associated fault propagation (e.g., Mitra, 1990; Erslev, 1991; Hardy and Ford, 1997; Allmendinger, 1998; Jabbour et al., 2012). These models better explain the wide variety of geometries documented at many fault-propagation anticlines (e.g., Gallup, 1954; Mitra, 1990; Xiao and Unsworth, 2006; Jabbour et al., 2012) (Fig. 2B).

2.3.1. Trishear kinematics

The trishear model successfully predicts the geometry of faults from surface data and successfully accounts for unit thickness and dip variations in relation to the rotating forelimb during progressive deformation (e.g., Erslev, 1991; Hardy and Ford, 1997; Allmendinger, 1998; Cardozo, 2005). There is a triangular region of high shear stress concentration in front of any propagating fracture or fault tip (Pollard and Segall, 1987), and the trishear model takes into account this variation in stress and resulting strain during fault-related deformation by defining a zone of distributed shear that expands ahead of a propagating fault tip (Fig. 2B; e.g., Hardy and Ford, 1997; Allmendinger, 1998; Cardoza, 2005). Fig. 2B (Stage 1) displays the key components of the trishear model for a propagating ramp fault, with a fixed footwall (velocity = 0) and a hanging wall that slips over that footwall at a given velocity (v_{hw}). Shear is distributed ahead of the propagating fault tip within the trishear zone at velocity values that vary from values approaching that of the hanging wall (v_{hw}), near the upper boundary of the trishear zone, to values approaching 0 (zero) near the lower boundary of the zone (Fig. 2B). To maintain area balance, a component of motion oblique to the fault must move material toward the footwall for all particles within the trishear zone of the system, a feature that distinguishes this model from one of simple shear (Erslev, 1991, Fig. 2B).

Fig. 2B displays consequences of trishear deformation upon bedded sedimentary strata as the fault propagates toward the surface. In this kinematic model, beds proximal to the propagating fault tip are more intensely deformed, with a greater shear gradient across the trishear zone resulting in a tighter anticlinal interlimb angle, while beds higher in the stratigraphic section display

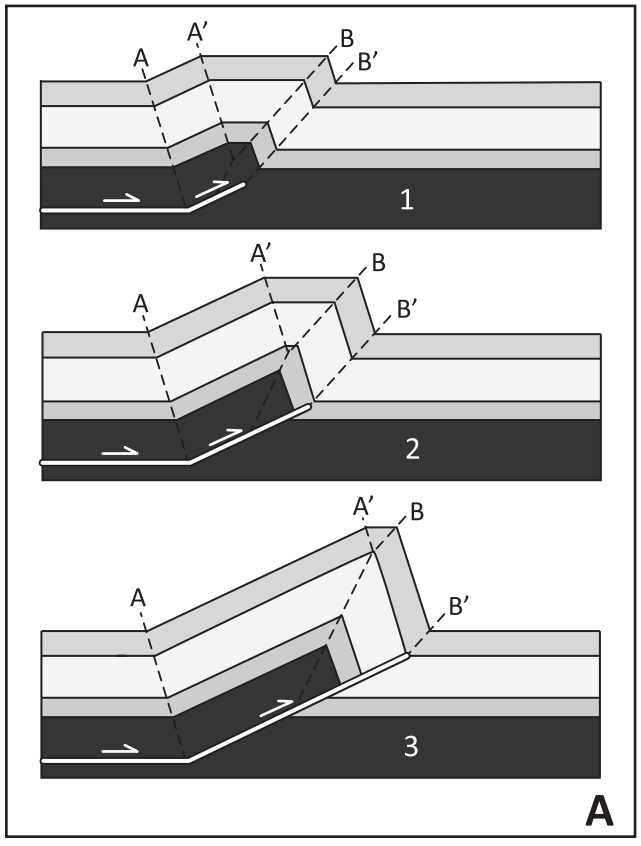

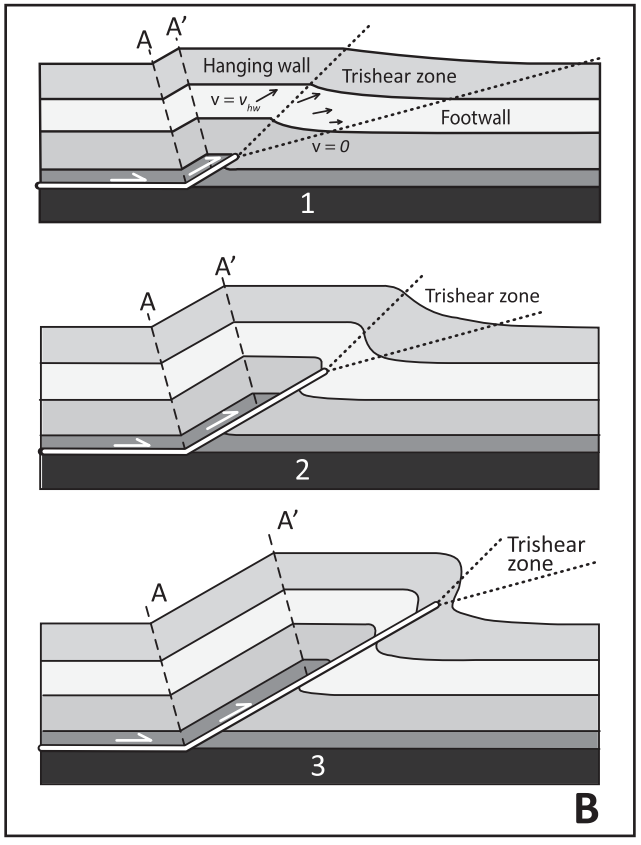

shallower bed dips (Fig. 2B). Importantly, the trishear zone itself migrates with the fault tip, commonly resulting in complex bed strains (Erslev, 1991), as the relative position of beds within the migrating trishear zone changes over time. Johnson and Johnson (2001) demonstrated that trishear kinematics are appropriate for fault-propagation-fold mechanics, with their mechanical analyses revealing velocity distributions consistent with trishear kinematics. As described in Section 3, our outcrop-scale and system-scale observations of contractional deformation are consistent with some elements of both kink-band and trishear kinematics.

3. Geologic and structural mapping of the Stillwell anticline

3.1. Mapping methods and study area access

We performed geologic and structural mapping of the Stillwell anticline using an integrated base map that included digitized 1:24,000 USGS topographic maps (Stillwell Mountain and Black Gap quadrangles), digital high-resolution (25 pixels/m) orthophotos, and USGS digital elevation models. We logged map data using a Trimble GeoXH handheld global positioning system receiver. We determined the spatial distribution of rock units in the field based on the lithologic characteristics defined by Maxwell et al. (1967) and St. John (1965, 1966), and we measured structural data, including bedding orientations, fold axes, axial planes, joint surfaces, fault surfaces, and slickenline lineations, using standard structural mapping techniques. We compiled all mapping and structural data with a combination of an integrated GIS database and digital maps. We augmented field descriptions and sketches with annotated field photographs of important structural features.

Most of the Stillwell anticline is located within the Black Gap Wildlife Management Area (BGWMA), to the east of Big Bend National Park (Fig. 1). Roads to the anticline can be accessed at the BGWMA headquarters, which is located on Texas Hwy. 2627, approximately 30 km (18 mi.) south of the Hwy. 2627 intersection with US Hwy. 385. The US 385 - TX 2627 intersection is 1.6 km (1 mi.) north of the Persimmon Gap entrance to Big Bend National Park. Contact the Black Gap Wildlife Management Area to apply for a permit to enter the area.

3.2. Map-view fold patterns and outcrop-based strain distribution

Based on previous work (e.g., St. John, 1965, 1966) and results presented here, the Stillwell anticline system is a NW-trending, asymmetric, moderately inclined, east-facing fold for much of its length (St. John, 1966; this study) (Fig. 3). The exposed geometries of the fold system are consistent with a fault-propagation anticline system formed primarily in the hanging wall of a subsurface fault system (e.g., Neely and Erslev, 2009) (Fig. 2). The topographic and structural expression of folding extends for nearly 10 km, measured

Fig. 2. Two models of fault-propagation fold evolution. A. Simplified diagram showing sequential kink-band kinematic deformation in front of an upward-propagating thrust ramp due to horizontal displacement along a decollement (modified from Suppe and Medwedeff, 1990). Note the constant interlimb angle with increasing depth at any time period. Note also the constant interlimb angles as fault slip progresses (1–3). B. Simplified diagram showing sequential trishear deformation in front of an upward-propagating thrust ramp due to horizontal displacement along a decollement (modified from Jabbour et al., 2012, as redrawn from Allmendinger, 1998). The magnitude and direction of velocity vectors within the trishear zone (illustrated in the Stage 1 diagram) changes from similar to the hanging wall velocity (v_{hw}) at the upper boundary to nearly zero near the base of the trishear zone. Note that the length of the backlimb (A – A′) increases with increasing slip along the ramp of the fault system. Also, note the changing interlimb angle in the anticline as the forelimb steepens with progressive fault slip (1–3). See text for discussion.

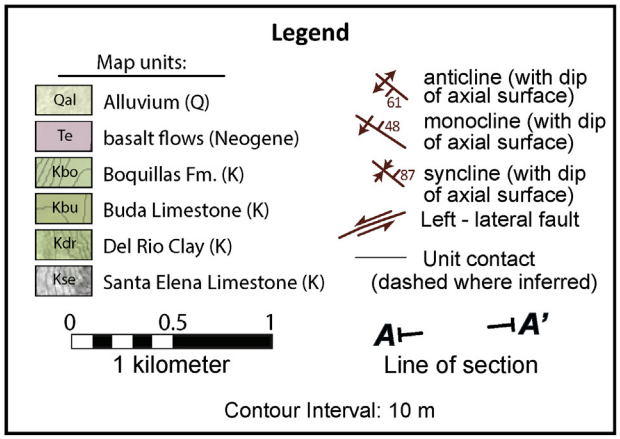

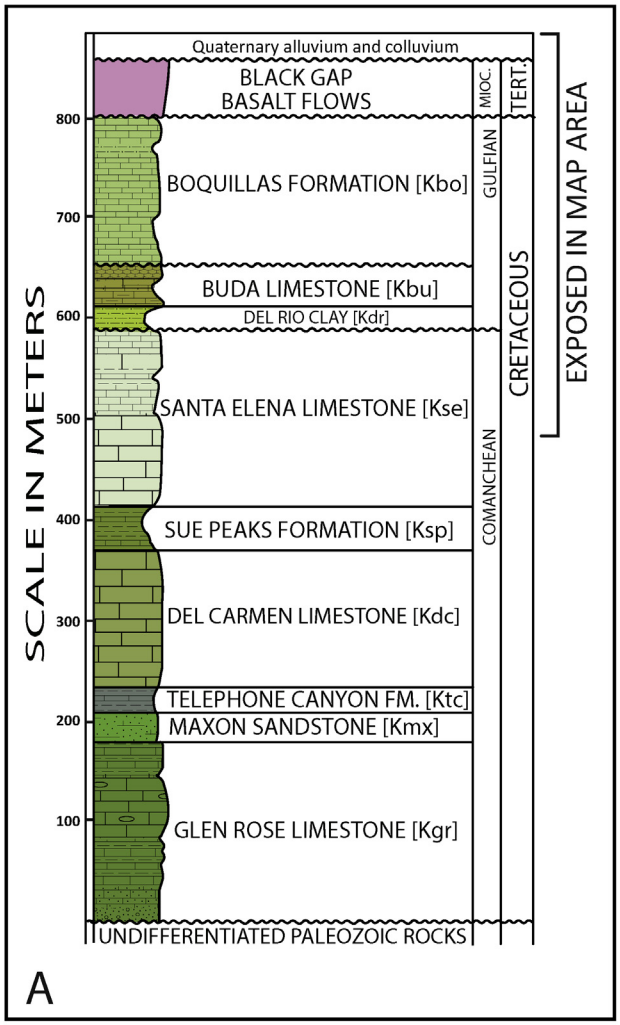

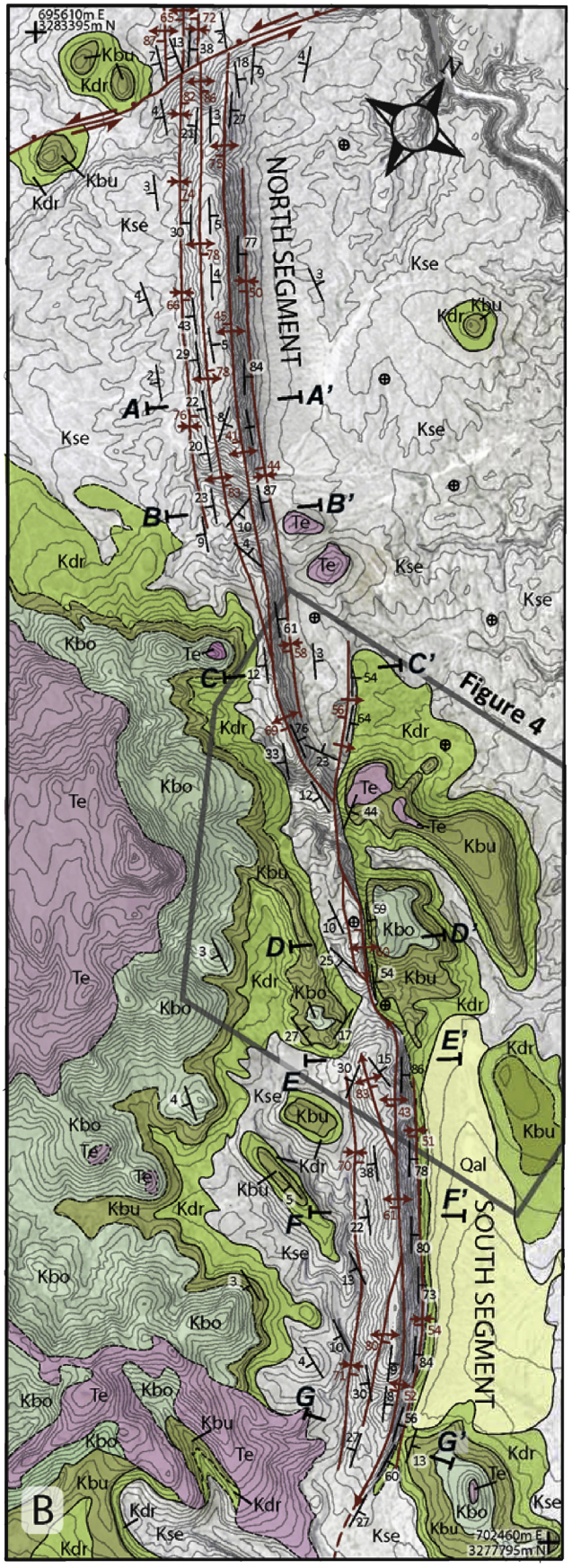

Fig. 3. A. Stratigraphy of the Stillwell anticline map area. Significantly modified from Cobb and Poth (1980), based on St. John (1965), Maxwell et al. (1967) and this study. B. Geologic map of the Stillwell anticline map area draped over orthophoto imagery. North and South segments of the anticline are shown, while the more complex central transition between segments is shown in Fig. 4 (indicated on map, right). Cross-sections A–A′ through G–G′ are shown in Fig. 8. Coordinates shown are from UTM Zone 13R.

along the fold's axial trace, and the structural geometries of the fold system are best defined by the well-bedded and resistant Santa Elena Limestone (Fig. 3). The less resistant Cretaceous Del Rio Clay and Buda Limestone (Fig. 3A) are best exposed to the northeast and southwest of the fold system (Fig. 3B), and the Cretaceous Boquillas Formation is best exposed to the southwest of the anticline, with only limited exposures of the unit to the northwest of the fold. Miocene-age basalt flows of the Black Gap Volcanic Field (Miggins, 2009) are present in the field area but do not obscure folding (Fig. 3B). Although the units stratigraphically above the Santa Elena Limestone help define fold geometries in a few locations, especially near the central region of the system, the middle and upper stratigraphy of the Santa Elena Limestone dominates most exposures of the anticline (Fig. 3).

Strain associated with the fold is limited to a relatively narrow region of approximately 500 m for much of the fold's length, with a shallow backlimb (<30° SW dip) and a steep forelimb (>50° NE dip) at most locations. We divide the anticline into three sections, including two relatively simple North and South segments and a more complex central transition zone (Fig. 3). In the central zone, the main trace of the anticline displays three left-stepping bends in the primary fold's axial trace (Fig. 4); these left steps appear to have localized erosion, with axis-perpendicular drainages that expose cross-sectional views at those locations. The greatest topographic relief (between the crest of the anticline and the area to the northeast) is located near the central sections of the North and South segments (Fig. 3). Together, these observations suggest some structural control on surficial processes such as erosion. There are no significant faults exposed in the field area, with the exception of the oblique normal-left-lateral fault, which displaces the northernmost exposure of the anticline system (Fig. 3B). This fault displays an apparent strike-slip displacement of approximately 300 m, with approximately 15 m of vertical throw related to normal displacement.

Our outcrop-scale investigation of the system indicates that most shear strain is focused within the forelimb at most locations (Fig. 5), with very few faults or other strain mechanisms affecting the backlimb or middle limb positions at any location along the

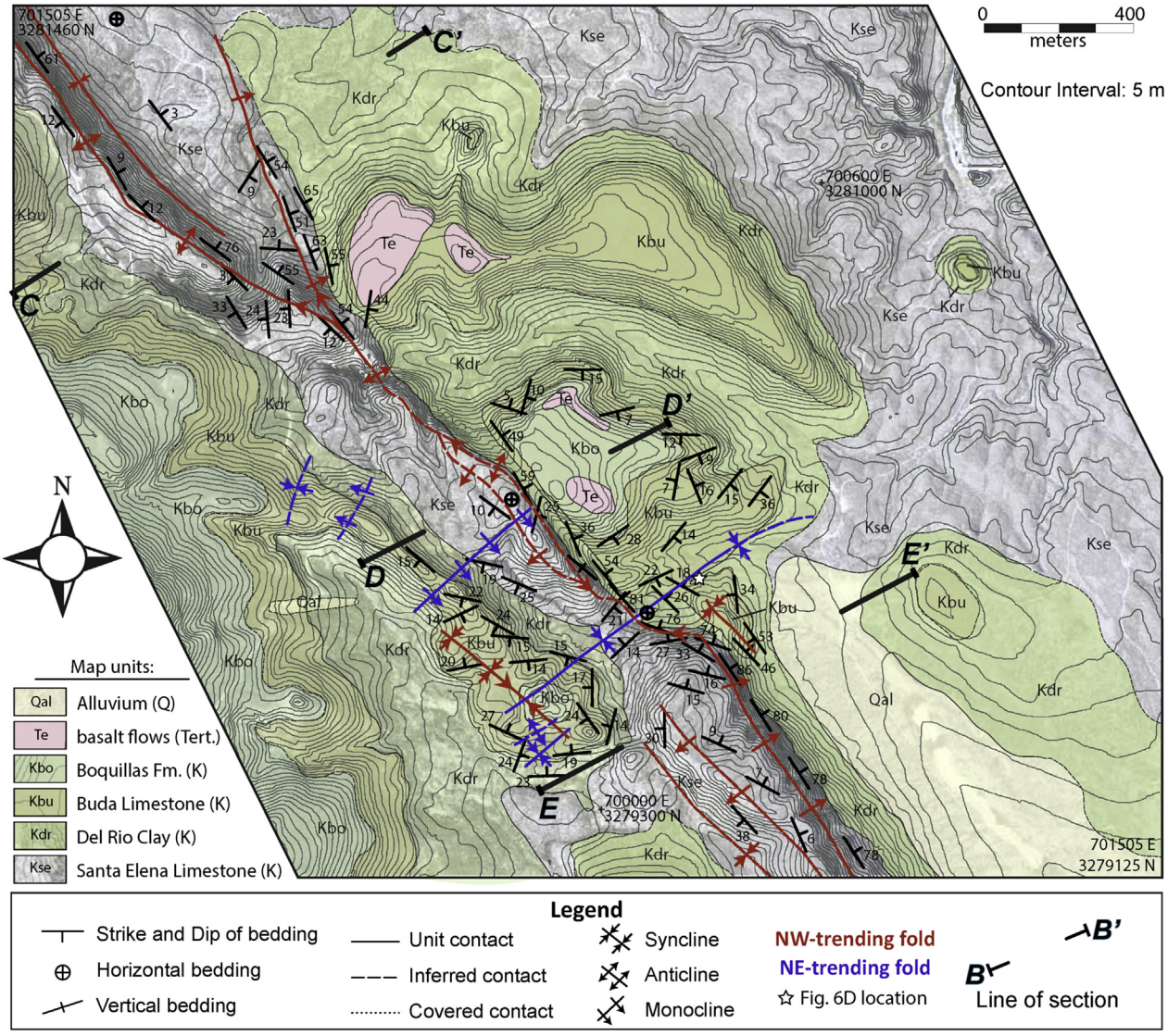

Fig. 4. Geologic map of the Stillwell anticline, focused on the left steps in the primary axial trace (see Fig. 4 for location). Cross-sections based on lines of section above are shown in Fig. 8. Location of outcrop shown in Fig. 6D is indicated by the white star near the longest syncline from the NE-trending fold set (in blue). Structural data (primarily strikes and dips) have been reduced in density (due to map scale reduction) to maintain clarity. Coordinates shown are from UTM Zone 13 R.

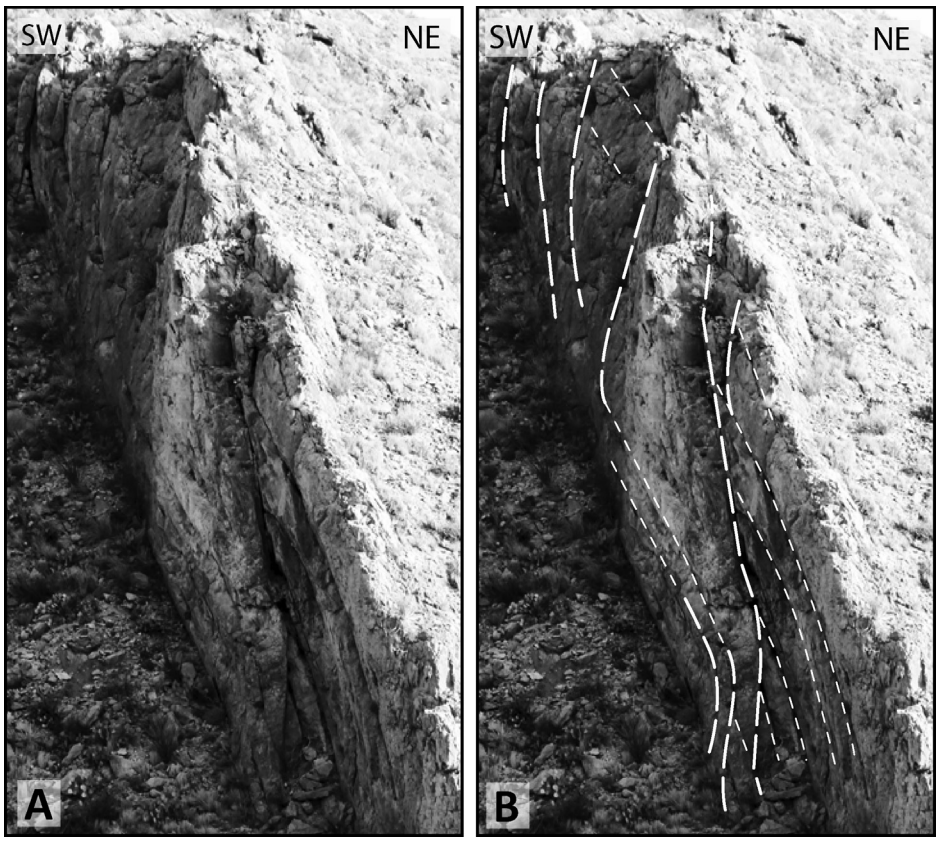

Fig. 5. Bedding and fault relationships in the forelimb of the Stillwell anticline system near line of section A–A′. Total height of outcrop shown is approximately 50 m. A. Outcrop exposure without bedding or faults indicated. B. Same photo as in A., displaying interpreted bedding and fault relationships. Faults are indicated by thick lines with long dashes, and beds are indicated by thin lines with short dashes. Significant fault slip has taken place along parting surfaces between bed planes, so the total displacements accommodated by these faults are not well constrained.

anticline system. At locations where the forelimb of the system is well exposed in cross section, ramp-flat geometries are common, with fault slip accommodated along bed partings and by faults that truncate bedding at low (20–40°) angles to the steeply dipping beds (Fig. 5). In exposures of the forelimb hinge, flexural slip processes, bed-parallel inter- and intra-layer slip, and cm-to meter-scale ramp-flat fault systems accommodate strain (Fig. 6), although the magnitude of shear strain is lower than within the forelimb. The bed-parallel slip observed within and between layers in the forelimb is also prominent in the forelimb hinge at most cross-sectional exposures of the anticline (Fig. 6B). At both structural positions (forelimb and forelimb hinge), slickenlines on exposed bedding surfaces provide evidence for bed-parallel slip, with lineation orientations consistent with displacements approximately perpendicular to the NW-trending anticline fold axis. In locations where we have documented meter-scale fault displacements in the forelimb, rocks adjacent to these faults commonly display intense fracturing (Fig. 6C), which rapidly decreases in intensity with distance from these discrete faults (to background levels within 0.5 m, measured perpendicular to the fault planes).

Importantly, beds within the weaker, more thinly-bedded Del Rio Clay display disharmonic, higher-order folds with orientations consistent with the dominant anticline system (Fig. 6D). Deformation documented in these lithologically weaker units suggests that units in the stratigraphy like the Sue Peaks Formation and the Del Rio Clay (Fig. 3A) accommodate strain in a manner that can be considered similar to ductile behavior on the scale of the anticline system. This behavior has implications for the propagation of faults in the subsurface.

3.3. Fold geometries of the North segment

Two significant cross-fold drainage systems expose excellent cross-sectional fold geometries in the North segment of the system (Figs. 3 and 4, and Fig. 7A–C). At most locations along the north section, topographic expression of the fold strongly mimics the resistant Santa Elena Limestone beds exposed along the anticline system. The dominant fold geometry across most of the north segment is displayed in Fig. 7A, a photograph from the same approximate position as cross-section A – A′ (Fig. 3). At most locations in the North segment of the system, the backlimb of the fold system dips southwest at 25–30°, the long (150–200 m) middle limb of the system dips shallowly (5–10°) toward the northeast, and the forelimb dips steeply (75–90°) toward the northeast (Figs. 3, 4 and 7) (note that dips shown in photographs are not true dips due to differences in perspective). However, near the north end of the study area, the topographic expression of the fold and the magnitude of dips in both the backlimb and forelimb decrease over less than 1 km, parallel to the fold axis, so that the fold displays backlimb dips of only 5–15° and forelimb dips of only 25–40° (Fig. 3). To the south of cross-section A – A′ in the North segment, the fold geometries also change over a relatively short axis-parallel distance.

Approximately 300 m south of the exposure shown in Fig. 7A, B displays the northwest-facing exposure of the anticline (image reversed for ease of comparison). This exposure shows a shorter middle limb (130 m vs. 150 m) with a change in dip direction (dips east at 10°) and a similarly steep forelimb. The change in dip direction of the middle limb of the system is coincident with a gentle plunge in the anticlinal axis toward the southeast (Fig. 3). Further

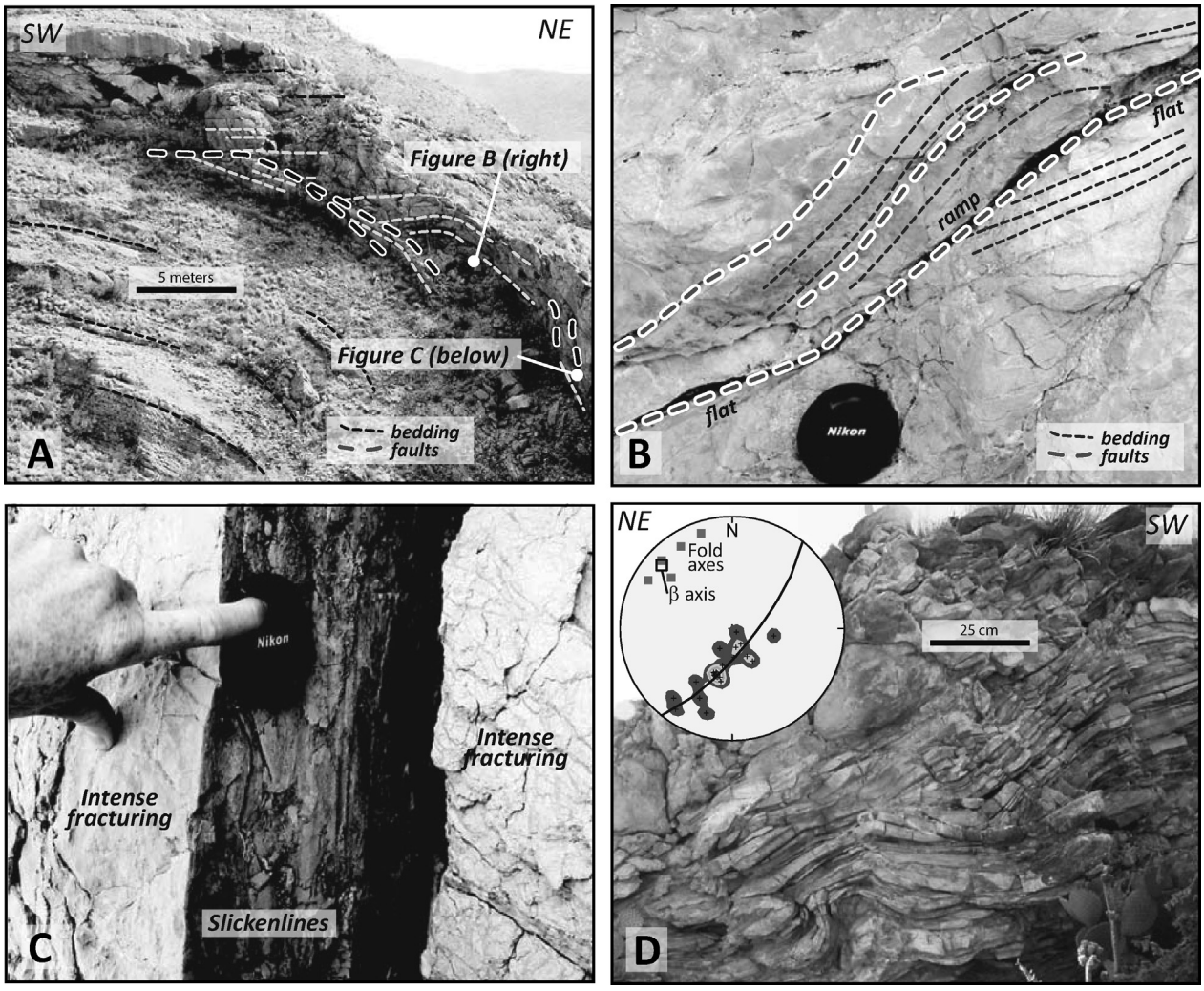

Fig. 6. Deformation styles across a range of scales. (A) Fault and bed relationships in the hinge, near B – B′ (Fig. 3), where bed-parallel slip and ramp-flat geometries are well-exposed (image reversed for clarity; forelimb to NE). The locations of B and C are indicated. (B) Ramp-flat geometries and duplex structures documented within a 1-m thick limestone bed, supporting a deformational history that involved brittle deformation and bedding-parallel slip across a range of scales. (C) Intense fracturing adjacent to a fault in the forelimb of the Stillwell anticline. (D) Disharmonic folding in the Del Rio Clay, at an exposure to the NE of line of section E–E′ (see white star for location on Fig. 4). Stereonet displays measured fold axes (squares) and density contoured poles to bedding planes, which define a gently NW plunging fold, coincident with folds directly measured. Higher-order folding documented here is consistent with the dominant Stillwell anticline system, and the plunges of the fold axes are consistent with the position of the outcrop on the SE limb of the NE-trending syncline (Fig. 4).

southeast on the anticline, just to the south of B – B′, the exposed middle limb decreases in length to only 50 m, with similar dip magnitudes in both backlimb and forelimb. These observed changes in middle limb length may be due, in part, to differences in stratigraphic position, with slightly deeper stratigraphic levels of the Santa Elena Limestone exposed moving southeast from near A – A′ to near B – B′.

Near the southern end of the North segment, the middle limb of the anticline disappears, with just a shallow to moderately-SW-dipping backlimb and a steeply dipping forelimb (Fig. 3). To the south of section C – C′, a cross-fold drainage reveals the geometry characteristic of the southernmost section of the North segment (Fig. 7D), where there is no clearly defined middle limb of the fold system.

3.4. Fold geometries of the South segment

Similar to the North segment of the system, fold geometries of the South segment of the system are well defined topographically by the resistant Santa Elena Limestone. Along the southern and northern sections of the South segment of the fold system, the dominant geometry is characterized by a moderately (25–30°) -SW-dipping backlimb, a shallowly (5–10°) -NW-dipping middle limb, and a steeply (55–85°) -NW-dipping forelimb (Fig. 7F, from cross-section G – G′). These geometries are consistent with the dominant geometry of the North segment of the fold system (see Fig. 7A for comparison), with only the central section of the South segment displaying some variation on this geometry. There, the middle limb of the system is no longer present (note the geometric transition from G-G- to F–F′ in Fig. 3), and the topographic relief of the exposed fold is perhaps greater than at any other location along the axial trace of the system (Fig. 3). There, the fold geometry is defined by a 20–40° SW-dipping backlimb and an ~80° NE-dipping forelimb. Near the southern border of the study region, the topographic and structural expression of the fold decreases over a relatively short distance (<400 m), and the dip of the forelimb shallows to less than 30° over that same distance (Fig. 3). Near the northern section of the South segment, the middle limb again

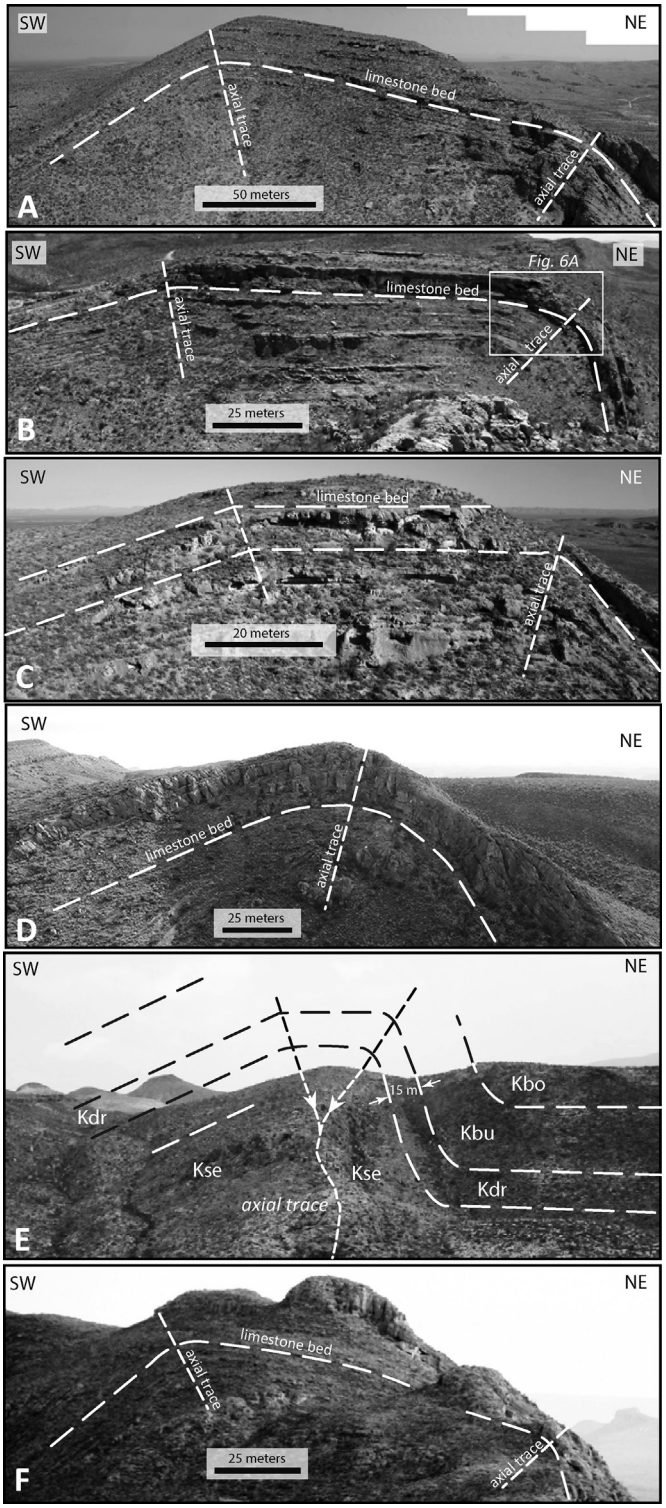

Fig. 7. Exposed cross-sectional geometries of the Stillwell anticline, as defined by the well-bedded Santa Elena Limestone, from north (A) to south (F). A. Cross-sectional exposure characteristic of most of the Northern segment of the anticline system, near A–A′ (Fig. 3). B. Cross-sectional exposure immediately to the SE of that shown in A, near B–B′. Note the shallower dip and shorter middle limb relative to that in A. This image has been reflected for ease of comparison. C. Cross-sectional exposure immediately to the SE of that shown in B. Note the significantly shorter middle-limb length relative to that in B. D. Cross-sectional exposure in the transition between the Northern and Central segments of the anticline system, near C–C′ (Fig. 3). Although the orientations of the backlimb and forelimb are similar to those shown in A and B, above, there is no middle limb present. This image has been reflected for ease of comparison. E. Oblique perspective of section D – D′ (line of section is on ridge profile), displaying geometry similar to that shown in D, above. Fold axes plunge toward the SE, toward viewer; note change in fold geometry and left step in axial trace. F. Cross-sectional exposure characteristic of the southern portion of the Southern segment of the anticline system, near G–G′ (Fig. 3). Note the similarity with A. Due to variations in perspectives and distances from observer, scales for all images are approximate, and bed orientations on all images should not be considered true dips.

becomes apparent and is well-defined by cross-section E–E′ (Figs. 3 and 4).

3.5. Fold geometries of the central transition zone

Here we describe the fold system transition from the northern section of the South segment to the southern section of the North segment, best displayed in Fig. 4. Approaching the northernmost section of the South segment, the middle limb of the anticline increases in width to its widest point (~200 m) at cross-section E–E′ and displays bed orientations on the backlimb and middle limb consistent with a plunging fold system (Fig. 4). The anticline's trace to the southeast of E–E′ trends NW, but proximal to that cross-section, the fold axial trace bends toward WNW – ESE for approximately 250 m before returning to its dominant NW trend (Fig. 4). Coincident with this bend, the dominant fold axis changes from gently-plunging along the NW – trending segment of the fold to moderately plunging toward the midpoint of the WNW – ESE segment (Fig. 4).

Coincident with this left – step in the anticline's axis is the most prominent example of the NE-trending folds that define a second fold set, nearly perpendicular to folds associated with the dominant Stillwell anticline system (Fig. 4). A NE-trending monocline, immediately south of cross-section D – D′ (Fig. 4), is coincident with a change from the subhorizontally-plunging primary anticline's axis, to the north of that location, to a gently SE-plunging axis to the southeast of section D – D′. Fig. 7E displays the anticline geometry at D – D′, viewed looking toward the northwest, where the geometry is defined by bedding in the Santa Elena Limestone, the Del Rio Clay, the Buda Limestone, and the base of the Boquillas Formation. Note the plunging fold axis toward the observer as well as the left step in the axial trace. To the NW of cross-section D – D′, the axis transitions from a subhorizontal orientation to a shallow plunge to the WNW, coincident with the bifurcation of the main anticline's axial trace (Fig. 4). To the northwest of this bifurcation, two separate, subparallel folds consist of the dominant North segment anticline on the southwest and a monocline with similar vergence to the northeast (Fig. 4).

4. Cross-section construction and analysis

We utilized geologic and structural mapping results to construct eight cross-sections with no vertical exaggeration oriented approximately perpendicular to the Stillwell anticline fold axis (Fig. 8). We chose lines of section (Fig. 3) where structural data were most complete and where cross-sectional information would best aid in interpretation of the three-dimensional structure. Because we have no subsurface data across the fold system, our constructions display constant bed thicknesses and domains of constant dip with depth within the fold system. In addition, because we use fold geometries to constrain possible subsurface fault geometries, these cross sections do not include interpreted faults in the subsurface (Fig. 8).

4.1. Axis-parallel variations in fault-propagation folding

The geometry of layers above a flat-ramp thrust fault system will change in a predictable manner with increasing displacement

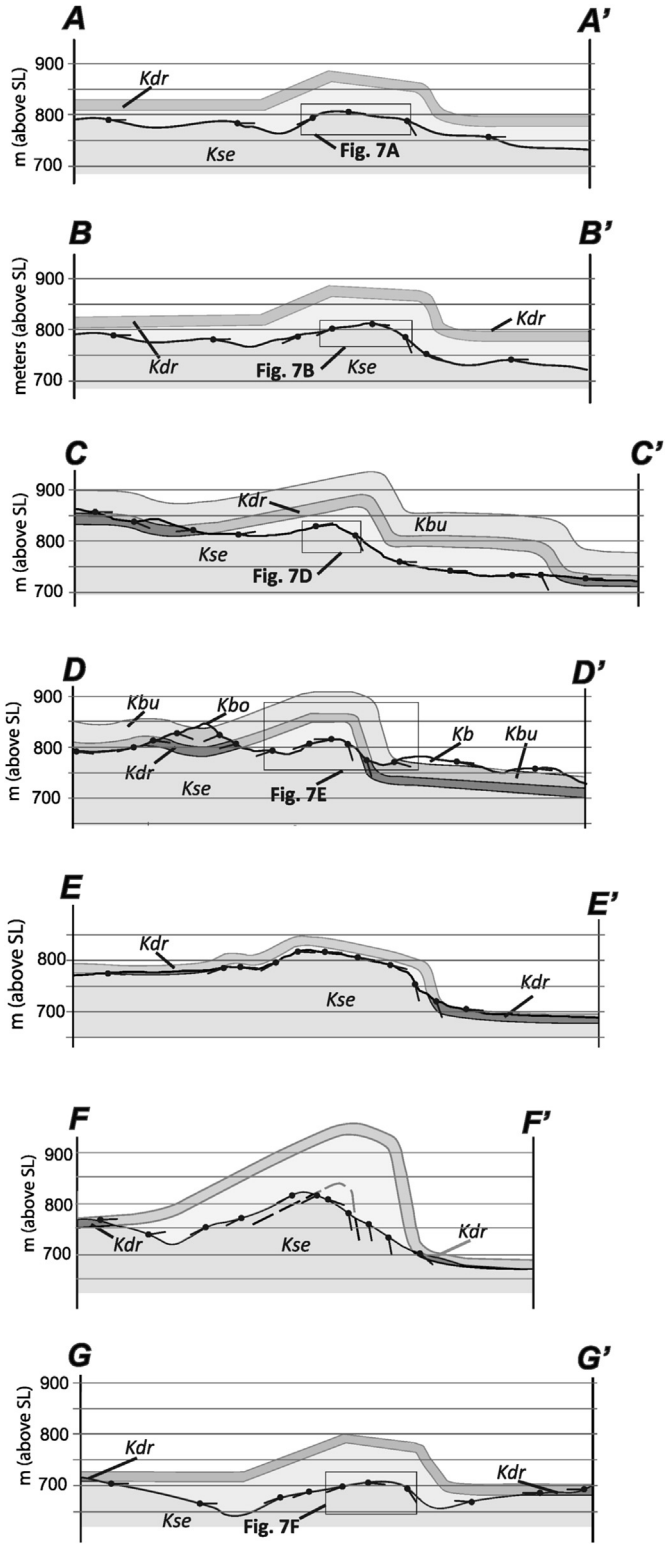

Fig. 8. Cross-sections constructed perpendicular to the axial trace of the Stillwell anticline. Bold black line is the topographic profile along each line of section, and ball-and-stick symbols indicate bedding dip. Refer to Fig. 3 for position of lines of section and for stratigraphy. Note the range in geometries represented along these lines of section. Unit thicknesses have been held constant, and no interpretations of subsurface fault geometry are shown. **Map units**: Kbo = Boquillas Formation (K) Kbu = Buda Limestone (K) Kdr = Del Rio Clay (K) Kse = Santa Elena Limestone (K). **No vertical exaggeration**.

(Fig. 2). We suggest that cross-sections (Fig. 8) reveal characteristics consistent with some aspects of both kink-band and trishear kinematic models. Importantly, in both models, the dip of the backlimb of a fault-propagation fold is parallel to the ramp of the fault system (Fig. 2), so for all cross sections in Fig. 8, we consider the backlimb angles to represent the subsurface fault ramp angles. In addition, these kinematic models dictate that the length of the backlimb increases with increasing slip along the ramp of the subsurface fault system. Therefore, although the magnitude of slip cannot be directly measured, backlimb length can be used to qualitatively compare slip magnitudes at different locations within the system. Cross sections from the North and South segments of the system (A – A′ and B – B′ from North segment; E–E′, F – F′, and G – G′ from South segment) display well-defined, SW-dipping backlimbs and steeply-NE-dipping forelimbs (Figs. 2, 3 and 8).

4.1.1. South segment

In the South segment, cross sections E–E′ and G – G′, near the northern and southern ends of the segment, respectively, display very similar geometries, with relatively short backlimb lengths and long, shallowly-NE-dipping middle limbs (Figs. 3 and 8). In contrast, section F – F′, near the center of the segment, displays a significantly longer backlimb, no defined middle limb, and greater fold amplitude than cross-section E–E′ or G–G′ (Figs. 3 and 8). The map-view axial traces show the absence of a significant middle limb for approximately 500 m in the middle of the Southern segment, centered on F – F′ (Fig. 3), with the bifurcation of the axial trace taking place 250 m to the northwest and southeast, revealing an increase in middle-limb length with increasing distance from the center of the segment (Fig. 3). These cross-sectional and map-view geometries support a model where maximum fault displacements produced fold geometries near the center of the segment, with decreasing fault displacements responsible for fold geometries approaching the ends of the segment (see stages 1–3 in Fig. 2A). Also, forelimb dip values (and fold amplitudes) decrease toward the southern end of the South segment, consistent with the trishear model of fault propagation, where forelimb dip angle decreases with decreasing slip on a propagating fault system (see stages 1–3 in Fig. 2B).

4.1.2. North segment

Cross sectional and map-view fold geometries from the North segment are remarkably consistent. Cross sections A – A′ and B – B′ display relatively similar backlimb dip values, with a slight decrease in the length of the shallowly-NE-dipping middle limb from A – A′ to B – B′, and steeply-NE-dipping forelimbs. To the north of A – A′, this geometry remains relatively constant until near the left-lateral-normal oblique slip fault (Fig. 3), where forelimb values and fold amplitude decreases over a relatively short (<300 m) distance, in a manner similar to that seen near the southern end of the South segment of the fold system. To the south of cross-section B – B′, the fold geometry changes as strain is likely accommodated by two subsurface faults instead of a single dominant fault.

4.1.3. Central transition zone

The more complex central zone (Fig. 4) reveals several features vital to understanding the temporal-spatial evolution of the system. In this zone, there are three prominent left steps in the axial trace of the dominant anticline system (Fig. 4), including: 1) a ~200 m left step immediately to the north of cross-section E–E′; 2) a ~150 m left step to the northwest of cross-section D – D′; and 3) a ~300 m left step associated with the bifurcation of the axial trace midway between lines of section D – D′ and C – C′.

As suggested by changes in fold geometry near the north end of the South segment of the anticline system (Section E–E′; Figs. 5 and

8) and map-view changes in bedding attitudes between E–E′ and D–D′, fold amplitude decreases approaching the first significant left step in the axial trace of the anticline system. Importantly, the axis of the fold system plunges toward each significant left step in the fold system (Figs. 3 and 4), suggesting a decrease in fold amplitude at those locations. Thus, we suggest that the NE-trending folds within the central transition zone formed passively, in response to the decreases in blind thrust fault displacement approaching each left step. In the central zone, those left steps also appear to have localized erosion, so that small drainage systems dissect the anticline at those locations. At D – D′ (Figs. 4 and 8), fold geometry is similar to other locations in the North and South segments, suggesting a single dominant subsurface fault system with a flat-ramp geometry and a vertical offset between areas to the NE and SW of the NW-trending anticline similar to the offset documented at other locations along the system.

Northwest of cross-section D – D′, the single fold bifurcates into two folds, with the axial trace of the monocline to the northeast maintaining a similar trend, while the axial trace of the fold to the southwest steps left nearly 300 m and becomes the dominant North segment fold (Fig. 4). Cross section C – C′ reveals that the monocline to the NE accommodates approximately 50 m vertical offset across the structure and displays a simple geometry potentially related to the hypothesized basement fault system (Section 4.2). The fold to the southwest displays a long, shallowly (12°) SW-dipping backlimb and a steeply NE-dipping forelimb consistent with fault-propagation fold formation. The total structural vertical offset across both folds is similar to the offset revealed by single folds at other locations (Fig. 8).

Similar to C–C′, cross-sections D–D′, and E–E′ also display evidence of multiple faults in the subsurface, with cross-sections D–D′ and E–E′ revealing low-amplitude folds to the southwest of the dominant anticline (Figs. 4 and 8). Thus, we suggest that the central transition zone represents a complex step-over between the dominant North and South segments of the anticline system, with fold geometries in cross-section and map view that are likely affected by multiple faults with axis – parallel changes in displacement.

4.2. Structural relief and basement fault reactivation

At all locations, cross-sections reveal vertical structural relief on the order of 50–100 m between the subhorizontal beds to the NE and SW of the NE-vergent anticline system (Figs. 3 and 8). This vertical relief is accommodated entirely within the Stillwell anticline system, over an axis-perpendicular distance of less than 500 m, with no folds that produce significant structural relief to the SW or NE of the anticline (Fig. 8). In addition, most middle limbs along the anticline system display shallow NE dips (Figs. 3 and 8), inconsistent with the expected horizontal middle limb of a flat-ramp fault propagation fold (Fig. 2) and dissimilar from the regional subhorizontal dip of beds located to the NE and SW of the NW-trending anticline (Figs. 3 and 8).

In order to explain these characteristics, we posit that the reverse reactivation of a basement-cored, steeply SW-dipping, planar (or only slightly listric), en echelon normal fault system controlled the initiation of the anticline system. We suggest that the fault must be planar because reactivation of a SW-dipping listric fault in the basement would produce SW-dipping beds over a wide area above the hanging wall of a reactivated listric fault, something we did not document in our field investigation (Fig. 3). In addition, the reactivation of a northwest – trending normal fault system is consistent with local and regional studies of tectonic reactivation of NW-trending structures (e.g., Muehlberger, 1980 *and refs. therein*; Muehlberger and Dickerson, 1989; Henry, 1998; Lehman and Busbey, 2007; Page et al., 2008) (Fig. 1).

Importantly, we suggest that a reactivated basement fault system and a shallower flat-ramp fault system (Section 4.1) could not have been kinematically linked. If these systems operated together, the upward-propagating basement fault would have refracted upon reaching a weaker stratigraphic horizon such as the Sue Peaks Formation (Fig. 3A), propagating along a decollement before ramping upward to generate the flat-ramp geometries described in Section 4.1. With increasing displacement on a single continuous system, both vertical structural relief and flat-ramp fault-propagation fold geometries would be generated at the same time. However, this would require that the basement fault propagate upward to the southwest of the anticline in order to link with the flat-ramp system, producing folds subparallel to the anticline system, which we have not documented in the study area. In addition, displacement along such bends in a fault system would produce a more complex fold pattern (e.g., Suppe, 1983) than we have documented here. Based on these observations, we suggest that formation of the Stillwell anticline system is best modeled using a two-stage kinematic process.

5. 2D trishear kinematic modeling

We used 2D forward kinematic modeling to test models of fault-propagation fold formation that best explain all structural data. The computer program FaultFold (formerly Trishear) utilizes trishear kinematics (e.g., Erslev, 1991; Hardy and Ford, 1997; Allmendinger, 1998; Allmendinger and Shaw, 2000; Zehnder and Allmendinger, 2000; Cardoza, 2005), described in Section 2.3.1. We suggest that the differences in fold geometries documented across the fold system represent temporal “snapshots” in the evolution of a fold, with geometries controlled by the magnitude of slip along a subsurface fault system. Therefore, we focused our modeling efforts on perhaps the best-constrained fold geometry in the anticline system, from cross-section A – A′ (Figs. 2 and 8), assuming that a successful coupled fault-fold model of this geometry would also explain most other geometries in the system. The backlimb of the anticline displays a 22° SW dip, a 150-m long middle limb with an 8° NE dip, a steeply-dipping forelimb, and a vertical offset between strata to the NE and SW of ~80 m. Our model tests suggest that a two-stage fault-propagation fold evolution satisfactorily explains most fold geometries along the anticline system.

5.1. Modeling basement fault reactivation

In our first stage of model testing, we modeled the reverse reactivation of a high-angle, SW-dipping normal fault (Section 4.2). The best models should produce a monocline with a shallow NE dip, consistent with the shallow NE middle-limb dips documented at many locations along the anticline system, including that from section A – A′. In addition, the total width of monoclonal tilt associated with the propagating reverse fault must be limited to less than 500 m to be consistent with field observations.

In the FaultFoldForward module of FaultFold, we built a stratigraphy consistent with the documented local section (e.g., Maxwell et al., 1967; St. John, 1965, 1966; this study), and we tested 32 first-stage models of fault-propagation folding. We kept the high-angle fault dip constant at 60°, the total slip constant at 92 m (based on the vertical throw of 80 m and the 60° fault dip), and we varied the trishear angle (see Stage 1 in Fig. 2B) from 25° to 40° and the propagation-to-slip (P/S) ratio from 1 to 2.5. Our best-fit model (Fig. 9A) reveals a dipping monoclinal limb that is approximately 315 m long with an 8° dip within at the stratigraphic level exposed on the surface today, consistent with the dip of the middle limb of

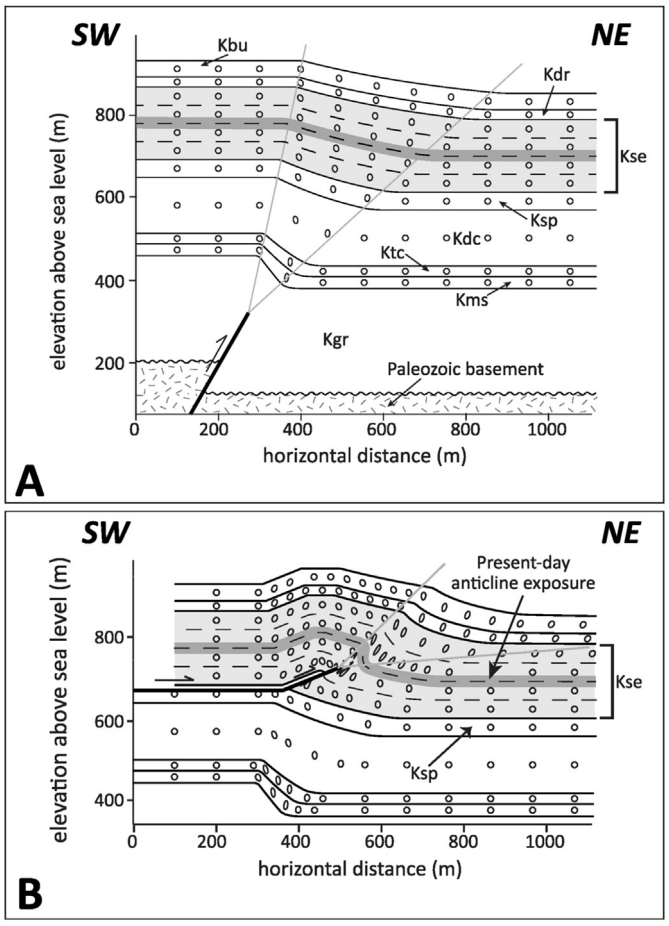

Fig. 9. A. Best-fit model of reverse reactivation of basement normal fault in Paleozoic basement. The finite geometry displayed here was created by 92 m total fault slip along a 60° SW-dipping fault with a trishear angle of 35° and a P/S (propagation/slip ratio) of 1.5. The dark gray layer within Kse represents the approximate position of the present-day exposure at cross-section A–A′ (Fig. 7A, and 8A). B. Best fit model of the stage 2 flat-ramp fault propagation, with a fault propagating along a detachment within the Cretaceous Sue Peaks Formation (Ksp) before propagating upward into the overlying lower Santa Elena limestone (Kse). See A. for identification of other units in the stratigraphy. The initial condition for this model was the best - fit model produced by the propagation of the high-angle basement fault shown in A. This model was produced by 100 m of total slip, with a ramp angle of 22°, a trishear angle of 30°, and a P/S value of 1.5. The dark gray layer within Kse represents the approximate position of the present-day exposure at cross-section A–A′ (Figs. 7A, and 8A).

the system at A – A′. Importantly, the finite geometry shown with FaultFoldForward displays strain ellipses, which represent the finite strain accommodated at different locations within the stratigraphy above the propagating fault. Our best-fit model suggests that the earlier stage of faulting likely did not produce any significant strain in the layers exposed today (Fig. 9B).

5.2. Modeling flat-ramp fault slip

Using the Stage 1 best-fit model (Fig. 9A) as the initial condition to model the initiation of the Stage 2 fault system, we tested models of a second fault system not kinematically linked to the first-stage, high angle fault. Our goal was to produce a fold system that most closely reproduces the geometries documented along cross section A – A′. Based on documented fold geometries and well-documented kinematic models (Fig. 2), we modeled the second stage of contraction as a fault that propagates along a horizontal detachment surface that ramps upward at an angle parallel to the backlimb angle (22° in section A – A′; Fig. 8). The variations in lithology in the local stratigraphy strongly support using the weak Sue Peaks Formation (Ksp; Fig. 3) as the horizontal plane, consistent with field-data that support ductile-like deformation within these weaker, thin-bedded units (see Del Rio Clay deformation in Fig. 6D). In our modeling, we assumed that the upper monocline hinge (formed during the first stage of fold formation) acted as a nucleation point for ramp propagation from the flat of the fault system, thus localizing second-stage fault-propagation folding across a narrow region relative to the fold axis.

The fault ramp angle was held constant 22° (backlimb angle of section A – A′), and we tested 152 forward models of fold evolution by varying trishear angle (from 30 to 60°), propagation-to-slip ratio (from 1 to 3), and total fault slip (from 80 to 200 m). Several combinations of parameter values resulted in models that closely approximated the documented cross-sectional geometry of section A – A′, so the best-fit model presented here (Fig. 9B) should not be considered unique (e.g., Allmendinger and Shaw, 2000; Cardoza, 2005). In this model, the trishear angle was 30°, the P/S ratio was 1.5, and the total fault slip was 100 m (Fig. 9B). Importantly, in all best-fit models, maximum finite strain is experienced in the forelimb of the system (see strain ellipses in Fig. 9B), consistent with field observations (Figs. 5 and 6).

6. Discussion and conclusions

Our work suggests that the initiation and early development of the Laramide-age Stillwell anticline system was fundamentally controlled by the reverse reactivation of a pre-existing, left-stepping, en echelon normal fault system in the Paleozoic basement. These high-angle reverse faults propagated upward into the overlying Cretaceous carbonate stratigraphy, initiating folding in the regions above the propagating faults. These results are consistent with other studies along the Laramide Orogeny that suggest localization of contractional deformation above reactivated basement structures (e.g., Miller et al., 1992, *and refs. therein*). Although neither these initial reverse faults nor the subsequent flat-ramp faults are exposed, the cross-sections of the Stillwell anticline display a complex array of geometries consistent with differing displacements on a subsurface flat-ramp fault system, with aspects of both kink-band and trishear kinematic models.

Fig. 10 reveals a sequence of cross-sections that display the coupled evolution of subsurface fault slip and overlying fold geometry that are consistent with cross-sections and kinematic model results from the Stillwell anticline system. In this model, fault slip occurs along a decollement within the Sue Peaks Formation and ramps upward at the hinge of the pre-existing monocline, propagating into the overlying Santa Elena Limestone. With increasing fault displacement, the overlying fold displays increasing backlimb length, decreasing middle limb length, increasing forelimb dip, and decreasing interlimb angle (Fig. 10). These changes are consistent with aspects of both kink-band and trishear kinematic models (Figs. 2 and 10). Our work suggests that interpreted cross-sections (Fig. 8) reveal “snapshots” of anticline development, consistent with the 3 stages shown in Fig. 10, from sections with low magnitude blind fault displacement of approximately 100 m (A–A′, B–B′, E′E′, and G–G′; Fig. 7) to moderate displacement on the order of 140 m (D – D′; Fig. 7) to high-magnitude displacement of approximately 180 m (F–F′; Fig. 7).

The maximum fault-propagation fold amplitude (Stage 3 in Fig. 10) is associated with the center of the South segment, and cross-sections along the central North segment display geometries consistent with lesser but still significant subsurface fault slip (Figs. 3, 8 and 10). Both the North and South segments displaying decreasing fold amplitude and assumed fault slip approaching

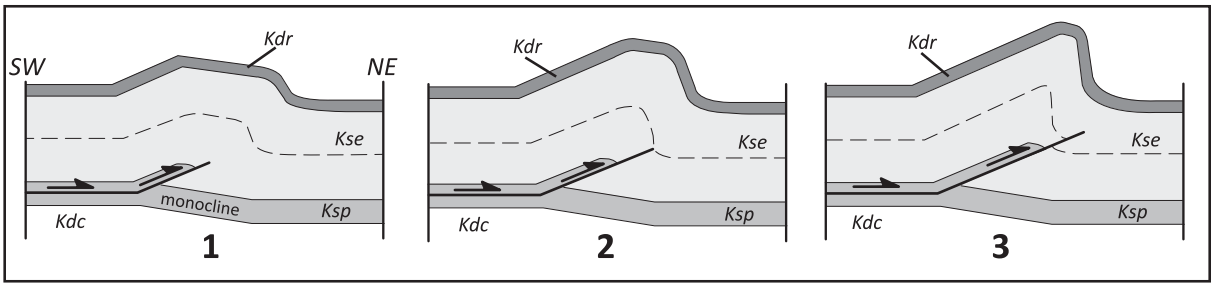

Fig. 10. Sequential fault-propagation fold evolution model for the Stillwell anticline. We developed this model based on cross-sections displayed in Fig. 8 and the results of trishear kinematic modeling. Prior to Step 1, the monocline related to basement normal fault reactivation has already formed. Cross-sections along the anticline system preserve displacement "snapshots" of the evolution of a fault-propagation fold: cross-sections A–A′, B–B′, E–E′, and G–G′ were used to build step 1; cross-section D–D′ was used to build step 2; and cross section F–F′ was used to build step 3. With increasing displacement on the flat-ramp fault system, backlimb length increases (consistent with both kink-band and trishear kinematic models), middle-limb length decreases (consistent with kink-band kinematics, Fig. 2A), forelimb dip increases (consistent with trishear kinematics, Fig. 2B), and interlimb angle decreases (consistent with trishear kinematics; Fig. 2B). See Fig. 3 for map unit abbreviations.

segment terminations (Figs. 3, 4 and 8). This finding is consistent with displacement gradients at the termination of contractional fault-related anticlines worldwide (e.g., Ratliff, 1992; Armstrong and Bartley, 1993; Fermor, 1999), where displacement decreases near the lateral fault tip, producing a plunging anticline.

This interpretation is also consistent with the position of the most significant NE-trending syncline in the central transition zone (Fig. 4). The syncline is likely controlled by the left step between the northernmost South segment and the segment near D – D′. The documented plunge of NW-trending anticlinal segments toward this left step (Fig. 4) is expected where a loss of displacement occurs in the relay zone between subsurface fault segments (e.g., Wilkerson et al., 2002; Ravaglia et al., 2004). It is likely that the total subsurface fault displacement at that location is lower than at any other location along the Stillwell anticline (excluding the terminations of the fold to the northwest and southeast of the system). Similarly, where the fault system bifurcates between cross-sections D – D′ and C – C′ (Fig. 4), both the primary anticline axis and the monocline axis plunge to the NW, supporting a model where for the length of the monocline, total fault displacement is shared between two subsurface faults as opposed to being accommodated by a single dominant blind fault.

In addition, our field observations and 2D kinematic modeling data suggest that fold geometry can be used to predict the cross-sectional distribution of strain across a contractional fault-propagation fold system. These data support a model where nearly all significant strain is focused within the forelimb of the fold system, with lesser strain in the middle limb-forelimb hinge of the system, and very little significant strain accommodated at other structural positions within the system. These findings are consistent with previous studies that have investigated how strain is accommodated in the zone of shear in front of a propagating fault tip (e.g., Pollard and Segall, 1987; Cooke and Pollard, 1997; Johnson and Johnson, 2001) but differ from studies that have found a direct relationship between layer curvature and strain (e.g., Hennings et al., 2000; Masaferro et al., 2003). Our field observations suggest that within the stronger units of layered carbonate systems (the Santa Elena Limestone in this study), strain in the forelimb of a fault-propagation fold is partitioned between a combination of interlayer slip, ramp-flat geometries across a range of scales, and intense fracturing adjacent to at least some zones of interlayer slip (Figs. 5 and 6). In weaker, thinner bedded and more clay-rich layers, however, disharmonic detachment folding would likely accommodate some percentage of this strain (Fig. 6D), likely reducing the percentage of strain accommodated by interlayer slip and/or fracturing.

We suggest that the spectacularly well-exposed Stillwell anticline system reveals an impressive array of cross-sectional exposures and map-view geometries that can be applied to other less well-exposed surface or subsurface fault-propagation fold systems. Our three-dimensional analysis of the Stillwell anticline system has yielded several important findings: 1) the two-stage formation, with very localized but contrasting styles (basement-cored vs. thin-skinned with flat-ramp geometries) of folding is unusual relative to other folds along the Laramide Orogeny; 2) variations in both map-view and cross-sectional fold geometries are strongly linked to the position of, the geometry of, and the slip accommodated by underlying fault systems; 3) shear strain in similar fault-propagation fold systems should be focused primarily along the forelimb of the system; and 4) this work provides context for future studies of fracture intensity within the folded carbonate rocks of the Stillwell anticline system.

Acknowledgments

Most of this work was funded by a grant from the National Science Foundation (EAR-PUI grant 1220235), with portions of fieldwork, transportation, student support, and laboratory analyses funded by the Trinity University Department of Geosciences. Thanks especially to insightful reviews by Joe Satterfield and Juliet Crider, which significantly improved the presentation of this study. Thanks also to Luciana de la Rocha, Daniel Hoin, Brett Mays, Lauren Mercado, Mark Mlella, Kristine Quiroz Purcell, Rebecca Schauer, and Sarah Wigginton, Trinity University undergraduates who assisted in field investigations and subsequent analyses. Special thanks to all of the staff at the Black Gap Wildlife Management Area, Brewster County, Texas, including Travis Smith, Dewey Stockbridge, Mike Pittman, and Mark Garrett. Thanks also to Tony Perez and Denise Wilson, who aided in the planning and execution of fieldwork.

References

Albritton Jr., D., Smith Jr., J., 1957. The Texas lineament: proceedings. In: Twentieth International Geological Congress, Mexico City, pp. 501–518 sec. 5.
Allmendinger, R., 1992. Fold and thrust tectonics of the western United States, exclusive of the accreted terranes. In: Burchfiel, B., Lipman, P., Zoback, M. (Eds.), The Cordilleran Orogen: Conterminous, vol. G-3. U.S. Geological Society of America, pp. 583–608.
Allmendinger, R.W., 1998. Inverse and forward numerical modeling of trishear fault-propagation folds. Tectonics 17 (4), 640–656.
Allmendinger, R.W., Shaw, J.H., 2000. Estimation of fault propagation distance from fold shape: implications for earthquake hazard assessment. Geology 28, 1099–1102.
Armstrong, P.A., Bartley, J.M., 1993. Displacement and deformation associated with a lateral thrust termination, southern Golden Gate Range, southern Nevada, USA. J. Struct. Geol. 15, 721–735.
Berge, T., 1981. Structural evolution of the Malone Mountains. University of Texas at Austin, Hudspeth County, Texas, p. 95. M.S. Thesis.

Cardozo, N., 2005. Trishear modeling of fold bedding data along a topographic profile. J. Struct. Geol. 27, 495–502.
Carpenter, D., 1997. Tectonic history of the metamorphic basement rocks of the Sierra del Carmen, Coahuila, Mexico. Geol. Soc. Am. Bull. 109, 1321–1332.
Chapin, C., Cather, S., 1983. Eocene tectonics and sedimentation in the Colorado Pleateau – Rocky Mountain area. In: Lowell, J. (Ed.), Rocky Mountain Foreland Basins and Uplifts. Rocky Mountain Association of Geologists Guidebook, pp. 33–56.
Chester, J.S., Chester, F.M., 1990. Fault-propagation folds above thrusts with constant dip. J. Struct. Geol. 12, 903–910.
Cobb, R., Poth, S., 1980. Superposed deformation in the santiago and northern del carmen mountains, Trans-Pecos Texas. In: Dickerson, P.W., Hoffer, J.M. (Eds.), Trans-Pecos Region, Southeastern New Mexico and West Texas.New Mexico Geological Society Fall Field Conference Guidebook, vol. 31, pp. 71–75.
Coney, P., Reynolds, S., 1977. Cordilleran Benioff zones. Nature 270, 403–406.
Cooke, M., Pollard, D., 1997. Bedding-plane slip in initial stages of fault-related folding. J. Struct. Geol. 19, 567–581.
Cullen, J., Knox, N.K., Crouch, J., Satterfield, J.I., 2013. Polyphase laramide structures and possible folded tertiary(?) Sills at Dagger Mountain, Big Bend National Park, Texas. Compass: Earth Sci. J. Sigma Gamma Epsilon 85, 98–119.
Dickinson, W., 1981. Plate tectonic evolution of the southern Cordillera. In: Dickinson, W., Payne, W. (Eds.), Relations of Tectonics to Ore Deposits of the Southern Cordillera, vol. 14. Arizona Geological Society Digest, pp. 113–135.
Erslev, E., 1991. Trishear fault-propagation folding. Geology 19, 617–620.
Erslev, E.A., Rogers, J.L., 1993. Basement-cover geometry of Laramide fault-propagation folds. In: Schmidt, C.J., Chase, R.B., Erslev, E.A. (Eds.), Laramide Basement Deformation in the Rocky Mountain Foreland of the Western United States, Geological Society of America Special Paper, vol. 280, pp. 125–146. Boulder, Colorado.
Fermor, P., 1999. Aspects of the three-dimensional structure of the Alberta Foothills and Front Ranges. Geol. Soc. Am. 111, 317–346.
Gallup, W.B., 1954. Geology of Turner Valley oil and gas field, Alberta, Canada. In: Clark, L.M. (Ed.), Western Canada Sedimentary Basins, pp. 397–414.
Goldhammer, R., Johnson, C., 1999. Mesozoic sequence stratigraphy and paleogeographic evolution of northeast Mexico. In: Bartolini, C., Wilson, J., Lawton, T. (Eds.), Mesozoic Sedimentary and Tectonic History of North-central Mexico, Geological Society of America Special Paper, vol. 340, pp. 1–58.
Gries, R., 1983. North-south compression of Rocky Mountain foreland structures. In: Lowell, J., Gries, R. (Eds.), Rocky Mountain Foreland Basins and Uplifts. Rocky Mountain Association of Geologists Guidebook, Denver, Colorado, pp. 9–32.
Hardy, S., Ford, M., 1997. Numerical modeling of trishear fault-propagation folding and associated growth strata. Tectonics 16, 841–854.
Hennings, P.H., Olson, J.E., Thompson, L.B., 2000. Combining outcrop data and three-dimensional structural models to characterize fractured reservoirs: an example from Wyoming. AAPG Bull. 84 (6), 830–849.
Henry, C.D., 1998. Geology of Big Bend Ranch State Park, Texas. In: Bureau of Economic Geology Guidebook, vol. 27. University of Texas at Austin, p. 72 geologic map scale 1:50,000.
Henry, C.D., Price, J.G., McDowell, R., 1983. Presence of the Rio Grande Rift in West Texas and Chihuahua. In: El Paso Geological Society Guidebook, vol. 15, pp. 108–118.
Henry, C.D., Price, J.G., 1985. Summary of the Tectonic Development of Trans-Pecos Texas. Miscellaneous Map No. 36. In: Bureau of Economic Geology, vol. 8. University of Texas at Austin. geologic map scale 1:500,000.
Henry, C.D., Price, J.G., 1986. Early Basin and Range development in Trans-Pecos Texas and adjacent Chihuahua – Magmatism and orientation, timing, and style of extension. J. Geophys. Res. 91 (B6), 6213–6224.
Jabbour, M., Dhont, D., Hervouet, Y., Deroin, J.-P., 2012. Geometry and kinematics of fault-propagation folds with variable interlimb angle. J. Struct. Geol. 42, 212–226.
Jacob, A.F., Albertus, R., 1985. Thrusting, Petroleum Seeps and Seismic Exploration, Front Range South of Denver, Colorado. In: AAPG Rocky Mountain Section Field Trip Guide. AAPG, Tulsa.
Johnson, K., Johnson, A., 2001. Mechanical analysis of the geometry of forced-folds. J. Struct. Geol. 24, 401–410.
Lehman, T.M., 1991. Sedimentation and tectonism in the Laramide Tornillo basin of West Texas. Sediment. Geol. 75, 9–28.
Lehman, T., Busbey, A., 2007. Society of Vertebrate Paleontology Fall 2007 Big Bend Field Trip Guide. Society of Vertebrate Paleontology, Austin, Texas, p. 117.
Liu, L., Gurnis, M., Seton, M., Saleeby, J., Muller, R., 2010. The Role of Oceanic Plateau Subduction in the Laramide Orogeny. http://dx.doi.org/10.1038/NGEO829. Nature Geoscience Letters.
Maler, M., 1990. Dead horse graben: a West Texas accommodation zone. Tectonics 9, 1357–1368.
Masafero, J.L., Bourne, R., Jauffred, J.C., 2003. 3D visualization of carbonate reservoirs. Lead. Edge 22, 18–25.
Maxwell, R., Lonsdale, J., Hazzard, R., Wilson, J., 1967. Geology of Big Bend National Park, Brewster County, Texas. Pub. 6711. In: Texas Bureau of Economic Geology, vol. 320. geologic map scale 1:62,500.
Mays, B., Surpless, B., Hoin, D., 2012. Kinematic Development of the Stillwell Anticline, West Texas. Southcentral Section GSA (Abstracts with Programs).
Mercier, E., Outtani, F., Frizon de Lamotte, D., 1997. Late-stage evolution of fault propagation folds: principles and example. J. Struct. Geol. 19, 185–193.
Miggins, D., 2009. Temporal and Geochemical Insights Related to Volcanic and Plutonic Activity within Big Bend National Park, Texas. Ph.D. Thesis. University of Texas at El Paso, El Paso, Texas, p. 309.
Miller, D., Nilsen, T., Bilodeau, W., 1992. Late Cretaceous to early Eocene geologic evolution of the U.S. Cordillera. In: Burchfiel, B., Lipman, P., Zoback, M. (Eds.), The Cordilleran Orogen: Conterminous, vol. G-3. U.S. Geological Society of America, pp. 205–260.
Mitra, S., 1990. Fault-propagation folds: geometry, kinematic evolution, and hydrocarbon traps. Am. Assoc. Pet. Geol. Bull. 74, 921–945.
Moustafa, A.R., 1983. Analysis of Laramide and Younger Deformation of a Segment of the Big Bend Region, Texas. Ph.D. Thesis. University of Texas at Austin, Austin, Texas, p. 278.
Moustafa, A.R., 1988. Structural geology of the Sierra del Carmen, Trans-Pecos, Texas. Geological Quadrangle Map GQ-0054. In: Bureau of Economic Geology, vol. 28. University of Texas at Austin. geologic map scale 1:48,000.
Muehlberger, W.R., 1980. Texas lineament revisited. In: New Mexico Geological Society Guidebook, 31st Field Conference, Trans-Pecos Region, pp. 113–121.
Muehlberger, W.R., Dickerson, P.W., 1989. A tectonic history of Trans-Pecos, Texas. In: Muehlberger, W.R., Dickerson, P.W. (Eds.), Structure and Stratigraphy of Trans-Pecos Texas. American Geophysical Union Field Trip Guidebook, vol. T315, pp. 35–54.
Neely, T., Erslev, E., 2009. The interplay of fold mechanisms and basement weaknesses t the transition between Laramide basement-involved arches, north-central Wyoming, USA. J. Struct. Geol. 31, 1012–1027.
Page, W., Turner, K., Bohannon, R., 2008. Tectonic history of Big Bend National Park. In: Gray, J., Page, W. (Eds.), Geological, Geochemical, and Geophysical Studies by the U.S, Geological Survey in Big Bend National Park, Texas. U.S. Geological Survey Circular, vol. 1327, pp. 3–13.
Pollard, D.D., Segall, P., 1987. Theoretical Displacements and Stresses Near Fractures in Rock: with Applications to Faults, Joints, Veins, Dikes, and Solution Surfaces. In: Fracture Mechanics of Rock, vol. 277, pp. 277–349.
Poole, F.G., Perry Jr., W.J., Madrid, R.J., Amaya-Martinez, R., 2005. Tectonic synthesis of the Ouachita-Marathon-Sonora orogenic margin of southern Laurentia: stratigraphic and structural implications for timing of deformational events and plate tectonic model. In: Anderson, T.H., Nourse, J.A., McKee, J.W., Steiner, M.B. (Eds.), The Mojave-Sonora Megashear Hypothesis: Development, Assessment, and Alternatives, Geological Society of America Special Paper, vol. 393, pp. 543–596.
Price, J.G., Henry, C.D., 1984. Stress orientations during Oligocene volcanism in Trans-Pecos: timing the transition from Laramide compression to basin and range tension. Geology 12, 238–241.
Price, J.G., Henry, C.D., 1988. Dikes in Big Bend National Park; petrologic and tectonic significance. In: Hayward, O.T. (Ed.), Centennial Field Guide 4, South-central Section of the Geological Society of America, pp. 435–440.
Ratliff, R.A., 1992. Deformation Studies of Folding and Faulting: Cross-section Kinematics, Strain Analysis, and Three-dimensional Geometry. Ph.D. thesis. University of Colorado.
Ravaglia, A., Turrini, C., Seno, S., 2004. Mechanical stratigraphy as a factor controlling the development of sandbox transfer zone: a three-dimensional analysis. J. Struct. Geol. 26, 2269–2283.
Rowan, M.G., Linares, R., 2000. Fold-evolution matrices and axial surfaces of fault-bend folds; application to the Medina Anticline, Eastern Cordillera, Columbia. AAPG Bull. 84, 741–764.
Savage, H., Cooke, M., 2003. Can flat-ramp-flat fault geometry be inferred from fold shape?: a comparison of kinematic and mechanical folds. J. Struct. Geol. 25, 2023–2034.
Sears, J., Price, R., 1978. The Siberian connection: a case for Precambrian separation of the North American and Siberian cratons. Geology 6, 267–270.
St John, B.E., 1965. Structural Geology of Black Gap Area, Brewster County, Texas. Ph.D. Thesis. University of Texas at Austin, Austin, Texas, p. 200.
St John, 1966. Geology of Black Gap Area, Brewster County, Texas. Geological Quadrangle Map GQ-0030. In: Bureau of Economic Geology, vol. 18. University of Texas at Austin. geologic map scale: 1:62,500.
Stone, D.S., 1993. Basement-involved thrust-generated folds as seismically imaged in the subsurface of the central Rocky Mountain foreland. In: Schmidt, C.J., Chase, R.B., Erslev, E.A. (Eds.), Laramide Basement Deformation in the Rocky Mountain Foreland of the Western United States, Geological Society of America Special Paper, vol. 280, pp. 271–318.
Suppe, J., 1983. Geometry and kinematics of fault-bend folding. Am. J. Sci. 283, 684–721.
Suppe, J., 1985. Principles of Structural Geology. Prentice-Hall, Inc., Englewood Cliffs, New Jersey, p. 537.
Suppe, J., Medwedeff, D.A., 1990. Geometry and kinematics of fault-propagation folding. Eclogae Geol. Helvetiae 83 (3), 409–454.
Surpless, B., DeZoeten, E., 2013. The Influence of Pre-existing Basement Structure on Laramide-age Contractional Deformation: Evolution of the Stillwell Anticline, West Texas. Southcentral Section GSA (Abstracts with Programs).
Surpless, B.E., Quiroz, K., 2010. Determining Subsurface Fault Geometry from Complex 3D Fold Patterns: Formation of the Stillwell Anticline, West Texas. American Geophysical Union. Abstracts with Programs, Abstract T51A-2022.
Thomas, W.A., 1991. The Appalachian-Ouachita rifted margin of southeastern North america. Geol. Soc. Am. Bull. 103, 415–431.
Thomas, W., 2011. The Iapetan rifted margin of southern Laurentia. Geosphere 7, 97–120.

Tweto, O., 1975. Laramide (Late Cretaceous – early Tertiary) orogeny in the southern Rocky Mountains. In: Curtis, B. (Ed.), Cenozoic History of the Southern Rocky Mountains, Geological Society of America Memoir, vol. 144, pp. 1–44.

Wilkerson, M., Apotria, T., Farid, T., 2002. Interpreting the geologic map expression of contractional fault-related fold terminations: lateral/oblique ramps versus displacement gradients. J. Struct. Geol. 24, 593–607.

Woodward, N., 1986. Thrust fault geometry of the Snake river range, Idaho and Wyoming. Geol. Soc. Am. Bull. 97, 178–193.

Xiao, W., Unsworth, M.J., 2006. Structural imaging in the Rock Mountain Fotthills (Alberta) using magnetotelluric exploration. Am. Assoc. Pet. Geol. Bull. 90, 321–333.

Zehnder, A.T., Allmendinger, R.W., 2000. Velocity field for the trishear model. J. Struct. Geol. 22, 1009–1014.